Supplementary Materials for

A sea change in our view of overturning in the subpolar North Atlantic

M. S. Lozier*, F. Li*, S. Bacon, F. Bahr, A. S. Bower, S. A. Cunningham, M. F. de Jong, L. de Steur†, B. deYoung, J. Fischer, S. F. Gary, B. J. W. Greenan, N. P. Holliday, A. Houk, L. Houpert, M. E. Inall, W. E. Johns, H. L. Johnson, C. Johnson, J. Karstensen, G. Koman, I. A. Le Bras, X. Lin, N. Mackay‡, D. P. Marshall, H. Mercier, M. Oltmanns, R. S. Pickart, A. L. Ramsey, D. Rayner, F. Straneo, V. Thierry, D. J. Torres, R. G. Williams, C. Wilson, J. Yang, I. Yashayaev, J. Zhao§

*Corresponding author. Email: mslozier@duke.edu (M.S.L.); feili.li@duke.edu (F.L.)
†Present address: Norwegian Polar Institute, Tromsø, Norway.
‡Present address: Department of Geography, University of Exeter, Devon, UK.
§Present address: University of Maryland Center for Environmental Science, Cambridge, MD, USA.

Published 1 February 2019, *Science* **363**, 516 (2019)
DOI: 10.1126/science.aau6592

This PDF file includes:

Materials and Methods

1. MOC, MHT and MFT calculations

Details of all calculation methods and of the observing system experiments run to test OSNAP methodology and array design are in Li *et al.* (*14*). Here we provide a brief summary.

a. MOC, MHT and MFT definitions
MOC is defined as the maximum of the overturning streamfunction in density space $\Psi(\sigma,t)$:

$$\mathrm{MOC}(t)=\max[\Psi(\sigma,t)]=\max\left[\int_{\sigma_{min}}^{\sigma}\int_{x_w}^{x_e} v(x,\sigma,t)\,dxd\sigma\right]\ (\mathrm{Sv}), \tag{S1}$$

where v, the velocity field normal to the OSNAP section, is integrated from west (x_w) to east (x_e) and from the top ($\sigma_{\min}$) across all density surfaces. We choose to calculate the MOC in density space in order to quantify the transformation of waters from one density class to another. The MOC upper (lower) limb is defined as the transport between the surface (bottom) and the density at which the overturning function reaches a maximum.

MHT is defined as:

$$\mathrm{MHT}(t)=\rho \mathrm{C_P}\int_{\sigma_{\min}}^{\sigma_{\max}}\int_{x_w}^{x_e} v(\sigma,t)\theta(\sigma,t)\,dxd\sigma\ \ [\mathrm{W}], \tag{S2}$$

where ρ is potential density, $\mathrm{C_P}$ is the specific heat of seawater, θ is potential temperature, and the double integral is taken over all σ surfaces and between the western and eastern boundaries.

MFT is defined as:

$$\mathrm{MFT(t)}=-\int_{\sigma_{\min}}^{\sigma_{\max}}\int_{x_w}^{x_e} v(\sigma,t)\frac{S(\sigma,t)-\bar{S}}{\bar{\mathrm{S}}}dxd\sigma\quad [\mathrm{Sv}], \tag{S3}$$

where $\bar{S}$ is the area-weighted section mean salinity (34.92 for the whole section, 34.85 for OSNAP West and 34.97 for OSNAP East), and the double integral is taken over all σ surfaces and between the western and eastern boundaries. The resultant MFT is an equivalent freshwater transport that can be interpreted as the volume of water at the section-mean salinity needed to balance the salt flux across the section in each 30-day period.

We follow the convention of positive (negative) values indicating northward (southward) volume (MOC), heat (MHT) and freshwater (MFT) transports.

b. Property and velocity fields
Property and velocity fields are calculated on a grid along the OSNAP section. The grid uses a Cartesian coordinate system with the x-axis parallel to the OSNAP line passing through all moorings, the y-axis perpendicular to that line, and the positive z-axis pointing upward. The horizontal resolution of this grid is ~1/4° and the vertical resolution is uniformly 20 m.

Mooring data in the boundary arrays are interpolated to estimate the temperature, salinity and density fields in these areas. Away from the arrays, gridded property fields are produced down to 2000 m via an objective analysis method based on temperature and salinity from Argo profiles, OSNAP gliders and moorings, and World Ocean Atlas 2013 (WOA13) temperature (*59*) and salinity (*60*) climatology. The WOA13 data are also used in the unmeasured areas on the Labrador and Scottish shelves (Figure 2 of Li *et al.*, *14*). Details on the validation of the objective analysis method can be found in previous studies (*14*, *41*). Below 2000 m, hydrographic data from 407 OSNAP CTD stations occupied during the summers of 2014 and 2016 are used to fill the grid. See complete cruise information at http://www.o-snap.org/observations/research-cruises/.

Mooring velocity data are interpolated to determine the velocity field in the boundary arrays. Away from the arrays, Ekman velocities calculated using ERA-Interim winds (*61*) are added to the surface Ekman layer, and geostrophic velocities are calculated with two different choices of reference depending on the availability of deep moorings. Where available, directly measured velocities at the top of deep moorings are used to provide the reference, with two exceptions: one in the western Labrador Basin and one in the central Iceland Basin. There, and in areas without deep moorings, the time-mean surface velocity (over the 21-month observational period) from satellite altimetry is used as the reference velocity. Because of the uncertainties of the surface velocities derived from satellite altimetry in the region (e.g., *62*, *63*), we use the altimetry-derived velocities to calculate a mean reference velocity only. For each time step, we use this mean reference velocity (only in the areas where we have no direct velocity measurements from moorings) and allow a compensation transport (see below) to determine the time-varying barotropic velocity.

For the unmeasured flow on the Labrador and Scottish shelves (see Figure 2 in Li *et al.*, *14*), we use climatological monthly velocities from a high-resolution (1/12°) regional ocean general circulation model. The model is the highest resolution member of the Family of Linked Atlantic Modeling Experiments (FLAME) ensemble that was developed for studying circulation in the Atlantic Ocean (*34, 64*). We repeated our calculations using climatological monthly velocities instead from a high-resolution (7 km) regional ocean-sea ice model (*65*) for the unmeasured flow above the Labrador shelf. This choice led to MOC, MHT and MFT estimates with negligible differences in the mean and in the variability. Future work includes improved estimates for these inshore properties and velocities.

c. Net throughflow

Our calculation assumes a zero net meridional mass transport across the entire OSNAP section. Long-term measurements across Davis Strait show a mean transport of -1.6 ± 0.2 Sv from the Arctic into the North Atlantic (*66*). To account for this transport, and still satisfy a zero-net-mass constraint across the entire section, we allow a transport of -1.6 ± 0.2 Sv across OSNAP West and then allow a compensating transport of the same magnitude but opposite sign across OSNAP East. When calculating the MOC at OSNAP West and East separately, we apply these same constraints.

Alternatively, we can require the net throughflow across the entire OSNAP section to be consistent with a recent estimate of 1.0 ± 0.05 Sv entering the Arctic from the Pacific (*67*) while keeping the 1.6 ± 0.2 Sv southward net transport at OSNAP West. Using these two constraints, we then apply a northward net transport of ~0.6 Sv across OSNAP East. As such, there is a mass

imbalance across the entire OSNAP section, matching the Bering Strait throughflow. This added constraint has only a minimal impact on the MOC estimate (14.5 ± 0.9 Sv) compared to a zero-net-throughflow across the entire section (14.9 ± 0.9 Sv). The two time series have a root-mean-square deviation (RMSD) of just 0.5 Sv and are strongly correlated (r= 0.997). Thus, for this study, we use the zero net meridional mass transport described above, but we continue to explore the best way to account for Pacific to Atlantic throughflows across the entire section, and OSNAP West and East separately.

d. Compensation transport

A compensation transport is added at each time step to ensure a zero net meridional mass transport across the entire OSNAP section (*14, 68*). That is, we use the constraint of zero net meridional mass transport to identify the fluctuating barotropic component of the flow. The mean compensation transport across the full array and its uncertainty over the observational period is -0.7 ± 3.3 Sv. This mean compensation transport is equivalent to adding a spatially uniform velocity of 0.04 cm/s across OSNAP West and -0.06 cm/s across OSNAP East to those areas without direct velocity measurements. The compensation velocity varies in time: the standard deviation of its time mean is 0.19 cm/s for OSNAP West and 0.44 cm/s for OSNAP East. To test the sensitivity of the MOC estimate to our distribution method, we also applied the compensation velocity uniformly across the whole section, which produced a nearly identical MOC estimate (14.8 ± 0.9 Sv). The two time series are highly correlated (r = 0.99) and have an RMSD of only 0.7 Sv. While a mean compensation transport of just -0.7 Sv is a strong validation of our methods, we continue to work on retrieving more accurate time-varying barotropic velocities and other ways to reduce this compensation transport and its uncertainty.

e. Mean and uncertainty estimates

We use Monte Carlo simulations to calculate estimates of the mean fluxes and to provide an estimate of the statistical uncertainty in those means. The statistical uncertainty stems from the intrinsic transport variability and random measurement uncertainty, and is typically dominated by the former (*69*). We note that all reported uncertainties indicate statistical uncertainty, and do not include possible bias errors, i.e., errors due to biases in Ekman transport or to deficiencies in array design or calculation methodology. A possible bias error of up to ~10% of the mean was found in Li *et al.* (*14*) based on Observing System Simulation Experiments (OSSEs) using a global ocean–sea-ice model. Further analysis will be performed for evaluating possible bias error at OSNAP and its sources.

For each 30-day period: We first create a field of variables used for the MOC, MHT and MFT estimates using the local (i.e., at each instrument site) 30-day mean and standard error for each variable at that site. These variables are temperature, salinity, velocity, sea surface height, wind stress, and the net throughflow across the subsection. For each Monte Carlo iteration, we randomly draw from these distributions to produce one realization of MOC (similarly for MHT and MFT). We continue the Monte Carlo iterations until the running mean of the flux estimate converges to within a prescribed value, ϵ, at which point the standard deviation of the mean has also converged (ϵ=1×10^{-3} Sv for MOC, 2×10^{-5} PW for MHT and 2×10^{-5} Sv for MFT). We use the average of all iterations as the mean flux for each 30-day period and report the standard deviation of the average as the uncertainty. Uncertainty in the 30-day mean estimates is ~ 4 Sv for MOC (Fig. 3), 0.1 PW for MHT (Fig. 4) and 0.1 Sv for MFT (Fig. 4).

To calculate the standard error of each variable, we divide the daily standard deviation by $\sqrt{30 \text{ days}/(2\tau)}$, where τ is the integral time scale (days) calculated from the autocorrelation function of the time series (*70*). We calculate the standard error for each variable at each point on the grid where appropriate. Depending upon the variable and location, τ ranges from a few days to a couple of months.

Over the entire 21-month observational record: To estimate the 21-month mean fluxes, that is the means over the entire observational record, and their uncertainty, we again employ Monte Carlo simulations. For each iteration, we create a 21-month MOC time series from the mean and standard error of each 30-day period, whose calculation is described above. We report the mean and standard deviation of 10,000 Monte Carlo estimates as the final 21-month mean MOC (14.9 Sv) and the corresponding uncertainty (0.9 Sv). The 21-month means and uncertainties for MHT and MFT are similarly obtained.

Alternatively, one can calculate the uncertainty in the 21-month mean as the standard deviation over the entire time period (Table S1) divided by $\sqrt{630 \text{ days}/(2\tau)}$. From the daily MOC time series, τ is estimated as 16 days, which yields 1 degree of freedom for every 32 days. The uncertainty that results from this calculation is 0.9 Sv, identical to that obtained from the Monte Carlo method.

2. Daily MOC estimates

Although daily measurements from all moored instruments are available, the objectively analyzed data product for temperature, salinity and density in the glider domain (see Fig. 2) is generated only every 30 days. The data product in this domain incorporates Argo and glider data, both with insufficient coverage to produce daily estimates. Thus, for our daily time series, we use daily measurements from all moored instruments, yet for the MOC calculation, the same density fields are used over the western flank of the Hatton Bank for each day during each 30-day period. For the MHT and MFT calculations, the same property fields are used in all areas without moored observations for each day during the 30-day period.

To test the extent to which the direct measurements (in the boundary currents) are responsible for the MOC variance at daily time scales, we reran the daily calculation using daily velocities from all moorings, yet we used the 21-month time-mean velocities for areas away from the mooring arrays. This calculation produces a very similar MOC estimate (a 0.7 Sv or ~4% difference) to that produced using time-varying velocities away from the arrays (r= 0.80 and RMSD= 3.3 Sv, using 10-day filtered data for both time series). Thus, we conclude that most of the daily MOC variability occurs in the directly measured boundary currents. Nonetheless, we report the MOC mean and uncertainty based on 30-day estimates, and only show the daily values to indicate the scale of variability on that time scale. We continue to refine the spatial and temporal resolution of the objectively analyzed fields so that in the future we will be able to report OSNAP flux estimates at time scales less than 30 days.

3. Alternative MOC definitions and coordinates

Use of potential density and depth coordinates

For the purpose of this study, the MOC is defined as the maximum of the overturning streamfunction in density space. Alternatively, the MOC can be defined as the maximum of the overturning streamfunction in depth space (maxMOC_z). The MOC using these two definitions is reported in Table S2 and shown in Fig. S1.

Use of neutral density coordinates

We also computed the MOC using neutral density surfaces (*71*) rather than potential density surfaces and found that the magnitude of the mean estimate was only marginally changed (15.3 ± 0.9 Sv compared to 14.9 ± 0.9 Sv using potential density surfaces; a 3% increase, well within the uncertainty estimate). The variability of the MOC time series created using neutral surfaces is indistinguishable from that using potential density surfaces (i.e., r= 0.996).

4. Decomposition of MHT and MFT into overturning and isopycnal components

The MHT and MFT across each OSNAP section are decomposed into overturning and isopycnal components (e.g., *20*) by first defining the total velocity, potential temperature and salinity as:

$$v(x,\sigma,t) =< v > (\sigma,t) + v'(x,\sigma,t) \ \ [m\,s^{-1}], \tag{S4}$$

$$\theta(x,\sigma,t) =< \theta > (\sigma,t) + \theta'(x,\sigma,t) \ \ [°C], \tag{S5}$$

$$S(x,\sigma,t) =< S > (\sigma,t) + S'(x,\sigma,t), \tag{S6}$$

where the angle brackets indicate a horizontal average at constant density and the prime indicates deviations from that average.

The MHT across each OSNAP section can then be divided into an overturning, $MHT_{overturning}$, and 'isopycnal' component, $MHT_{isopycnal}$, (see Fig. 4) as follows:

$$MHT_{overturning}(t) = \rho C_P \int_{\sigma_{min}}^{\sigma_{max}} \int_{x_w}^{x_e} < v > (\sigma,t) < \theta > (\sigma,t)\, dx d\sigma \ \ [W], \tag{S7}$$

$$MHT_{isopycnal}(t) = \rho C_P \int_{\sigma_{min}}^{\sigma_{max}} \int_{x_w}^{x_e} v'(x,\sigma,t)\, \theta'(x,\sigma,t)\, dx d\sigma \quad [W], \tag{S8}$$

where $\rho C_P = 4.1 \times 10^6 \ Jm^{-3}\, K^{-1}$, and the double integral is taken over all σ surfaces and between the western and eastern boundaries.

The MFT across each OSNAP section is similarly decomposed:

$$MFT_{overturning}(t) = -\int_{\sigma_{min}}^{\sigma_{max}} \int_{x_w}^{x_e} < v > (\sigma, t) \frac{< S > (\sigma, t)}{\bar{S}} dx d\sigma \quad [Sv], \tag{S9}$$

$$MFT_{isopycnal}(t) = -\int_{\sigma_{min}}^{\sigma_{max}} \int_{x_w}^{x_e} v'(x, \sigma, t) \frac{S'(x, \sigma, t)}{\bar{S}} \, dx d\sigma \quad [Sv]. \tag{S10}$$

The overturning and isopycnal components in density space for both MHT and MFT are shown in Fig. 4. The above decomposition can also be performed in depth space to yield an overturning and horizontal ('gyre') component, both shown in Fig. S2.

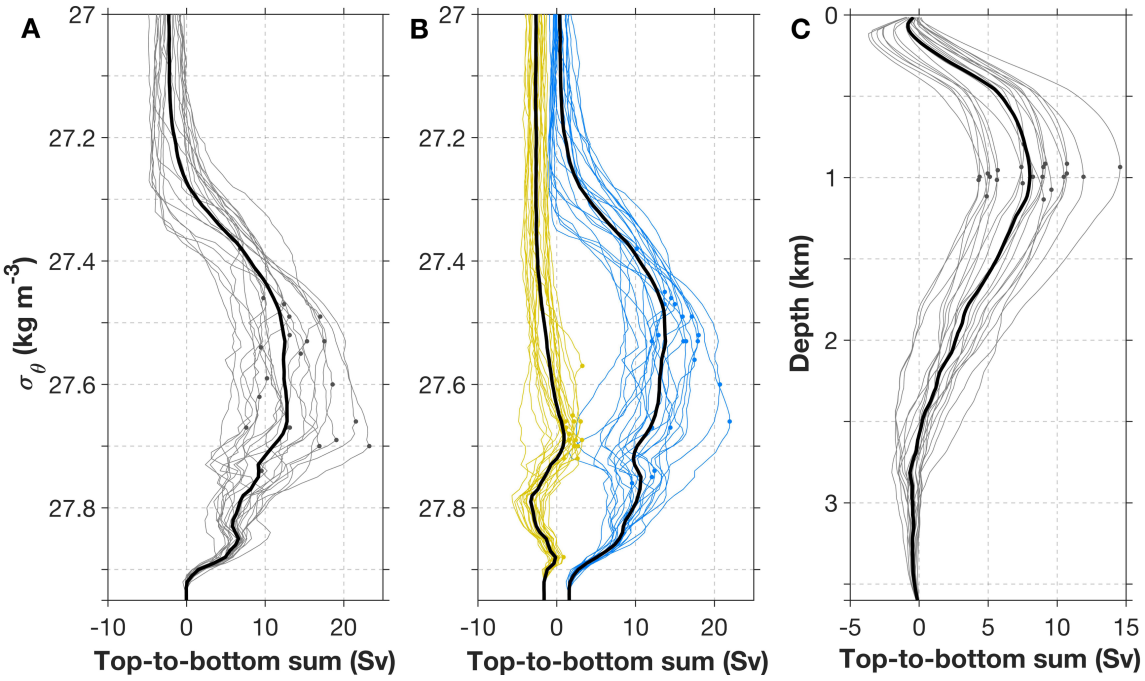

Fig. S1.

Streamfunction across the OSNAP section. Streamfunction in density space across the full array, (**A**) across the OSNAP West (yellow) and OSNAP East (blue) subsections (**B**), and in depth space across the full array (**C**). The 21 30-day means (thin lines) are shown in all panels, with the MOC (maximum of the streamfunction) denoted for each of the 21 profiles (dot). The 21-month mean streamfunction (thick solid lines in all panels) is obtained by averaging all 21 transport values within each density or depth bin. The potential densities corresponding to the maximum of the streamfunction across the subsections (27.69 kg m^{-3} for OSNAP West and 27.53 kg m^{-3} for OSNAP East) are slightly different from that derived from the mean streamfunction across the full array (27.66 kg m^{-3}). The vertical separation between the 27.69 and 27.66 kg m^{-3} isopycnals across OSNAP West is on average less than ~100 m, and the separation between the 27.53 and 27.66 kg m^{-3} isopycnals across OSNAP East is on average ~100-200 m. Note that the maximum value (i.e., the MOC) of the mean streamfunction in density space (thick lines in **A** and **B**) underestimates the mean of the 21 individual 30-day MOC estimates reported in the main text. Because the density at which the maxima occur varies over the record, the maximum of the averaged MOC streamfunction will be smaller than an average of the maximum MOC streamfunctions.

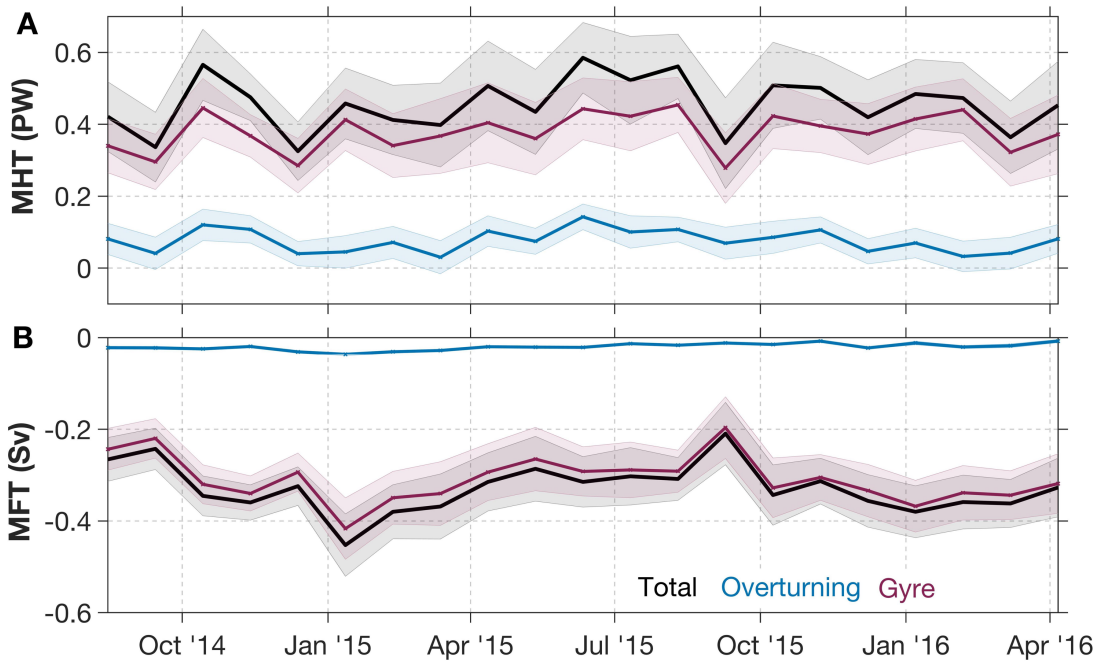

Fig. S2.

MHT and MFT across the OSNAP section. (**A** and **B**) Same as in Fig. 4, but with MHT (**A**) and MFT (**B**) decomposed in depth space into overturning (blue lines) and gyre (red lines) components.

Table S1.

Mean transport estimates with one standard deviation over the 21-month period. MHT estimates marked with '#' are temperature, rather than heat, transports since there is a net mass flux across these sections. All reported MFT values are equivalent freshwater transports (*14*). The standard deviations here reflect the monthly variability over the 21-month period (Fig. 3), not the uncertainty in the estimate of the mean. For the latter, please see Table S3.

	MOC (Sv)	**MHT (PW)**	**MFT (Sv)**
OSNAP	14.9 ± 4.1	0.45 ± 0.08	-0.33 ± 0.05
OSNAP East	15.6 ± 3.1	$0.38^{\#}$ ± 0.08	-0.14 ± 0.04
OSNAP West	2.1 ± 0.9	$0.080^{\#}$ ± 0.016	-0.184 ± 0.041

Table S2.

Comparison of MOC used in text to an alternative definition. The mean MOC and its uncertainty over the period from August 2014 to April 2016 using different MOC definitions and calculated using 30-day means. The first column is the metric used in the text, where MOC is defined as the maximum of the overturning streamfunction in density space (Figs. S1A and S1B). The second column, $maxMOC_z$, is the maximum of the overturning streamfunction in depth space (Fig. S1C).

	MOC [Sv]	**maxMOC_z [Sv]**
OSNAP	14.9 ± 0.9	8.0 ± 0.7
OSNAP East	15.6 ± 0.8	8.2 ± 0.6
OSNAP West	2.1 ± 0.3	0.8 ± 0.2

Table S3.

Compilation of MOC, MHT, MFT and Ekman transport estimates in the North Atlantic. Reported values are the time mean plus/minus an uncertainty estimate. MOC estimates marked with '*'are those calculated in depth space; otherwise, density space is used. MHT estimates marked with '#' are temperature, rather than heat, transports since there is a net mass flux across these sections. All reported MFT values are equivalent freshwater transports (*14*). Estimates are based on direct measurements from different time periods. The long-term mean RAPID-MOCHA MOC (M15a: *26*), MHT (*26*), MFT (M15b: *72*) and Ekman transport (M15a) are for April 2004 – October 2012, while the latest estimate of the MOC and Ekman transport during the overlap period with OSNAP are for 2014 – 2016 (S18: *21*). The uncertainties marked with '&' are calculated based on the reported uncertainties in the annual volume (0.9 Sv; M15a) and freshwater (0.02 Sv; M15b) transports. The OVIDE MOC estimate is for 1993 – 2010, while the OVIDE MHT is the mean summer estimate between 1997–2010 (*22*). There are two MOC estimates at 59.5°N: one is the 2002-2008 mean summer estimate (S12: *29*), the other is the long-term mean estimate between early 2012 to early 2016 (R17: *30*). The latter study also provided MHT and MFT estimates. The MOC estimated at AR7W is based on either repeat hydrography between 1990-1997 (P07: *25*) or Argo floats between March 2002 – April 2016 (H17: *28*).

	MOC (Sv)	MHT (PW)	MFT (Sv)	Ekman (Sv)
OSNAP	**14.9 ± 0.9**	**0.45 ± 0.02**	**-0.33 ± 0.01**	**-1.72 ± 0.02**
RAPID-MOCHA	17.2* ± 0.3$^{\&}$ (M15a) 16.8* ± 0.5$^{\&}$ (S18)	1.25 ± 0.11 (M15a)	-0.43 ± 0.007$^{\&}$ (M15b)	3.8 (M15a) 3.9 (S18)
OSNAP East	**15.6 ± 0.8**	**0.38$^{\#}$ ± 0.02**	**-0.14 ± 0.01**	**-1.51 ± 0.02**
OVIDE 59.5°N	18.1 ± 1.4 18.4 ± 3.4 (R17) 16.6 ± 1.1 (S12)	0.51$^{\#}$ ± 0.06 0.399$^{\#}$ ± 0.074 (R17)	-0.20 ± 0.04 (R17)	
OSNAP West	**2.1 ± 0.3**	**0.080$^{\#}$ ± 0.004**	**-0.184 ± 0.004**	**-0.18 ± 0.01**
AR7W	2 (P07) 1* (P07) 2.5 ± 0.75 (H17) 0.9* ± 0.5 (H17)	0.038 (P07)		

References and Notes

1. W. S. Broecker, *The Glacial World According to Wally* (Eldigio Press, ed. 2, 1995).

2. National Research Council, *Abrupt Climate Change: Inevitable Surprises* (National Academies Press, 2002).

3. S. A. Cunningham, T. Kanzow, D. Rayner, M. O. Baringer, W. E. Johns, J. Marotzke, H. R. Longworth, E. M. Grant, J. J.-M. Hirschi, L. M. Beal, C. S. Meinen, H. L. Bryden, Temporal variability of the Atlantic meridional overturning circulation at 26.5°N. *Science* **317**, 935–938 (2007). doi:10.1126/science.1141304 Medline

4. M. A. Srokosz, H. L. Bryden, Observing the Atlantic Meridional Overturning Circulation yields a decade of inevitable surprises. *Science* **348**, 1255575 (2015). doi:10.1126/science.1255575 Medline

5. R. J. Bingham, C. W. Hughes, V. Roussenov, R. G. Williams, Meridional coherence of the North Atlantic meridional overturning circulation. *Geophys. Res. Lett.* **34**, L23606 (2007). doi:10.1029/2007GL031731

6. M. S. Lozier, V. Roussenov, M. S. C. Reed, R. G. Williams, Opposing decadal changes for the North Atlantic meridional overturning circulation. *Nat. Geosci.* **3**, 728–734 (2010). doi:10.1038/ngeo947

7. R. G. Williams, V. Roussenov, D. Smith, M. S. Lozier, Decadal evolution of ocean thermal anomalies in the North Atlantic: The effects of Ekman, overturning, and horizontal transport. *J. Clim.* **27**, 698–719 (2014). doi:10.1175/JCLI-D-12-00234.1

8. J. Zhao, W. Johns, Wind-forced interannual variability of the Atlantic meridional overturning circulation at 26.5°N. *J. Geophys. Res. Oceans* **119**, 2403–2419 (2014). doi:10.1002/2013JC009407

9. I. Polo, J. Robson, R. Sutton, M. A. Balmaseda, The importance of wind and buoyancy forcing for the boundary density variations and the geostrophic component of the AMOC at 26°N. *J. Phys. Oceanogr.* **44**, 2387–2408 (2014). doi:10.1175/JPO-D-13-0264.1

10. A. Biastoch, C. W. Böning, J. Getzlaff, J.-M. Molines, G. Madec, Causes of interannual–decadal variability in the meridional overturning circulation of the midlatitude North Atlantic Ocean. *J. Clim.* **21**, 6599–6615 (2008). doi:10.1175/2008JCLI2404.1

11. IPCC, *Climate Change 2013: The Physical Science Basis*, T. F. Stocker, D. Qin, G.-K. Plattner, M. Tignor, S. K. Allen, J. Boschung, A. Nauels, Y. Xia, V. Bex, P. M. Midgley, Eds. (Cambridge Univ. Press, 2013).

12. G. A. McKinley, A. R. Fay, N. S. Lovenduski, D. J. Pilcher, Natural variability and anthropogenic trends in the ocean carbon sink. *Annu. Rev. Mar. Sci.* **9**, 125–150 (2017). doi:10.1146/annurev-marine-010816-060529 Medline

13. M. Susan Lozier, S. Bacon, A. S. Bower, S. A. Cunningham, M. Femke de Jong, L. de Steur, B. deYoung, J. Fischer, S. F. Gary, B. J. W. Greenan, P. Heimbach, N. P. Holliday, L. Houpert, M. E. Inall, W. E. Johns, H. L. Johnson, J. Karstensen, F. Li, X. Lin, N. Mackay, D. P. Marshall, H. Mercier, P. G. Myers, R. S. Pickart, H. R. Pillar, F. Straneo, V. Thierry, R. A. Weller, R. G. Williams, C. Wilson, J. Yang, J. Zhao, J. D. Zika,

Overturning in the Subpolar North Atlantic Program: A new international ocean observing system. *Bull. Am. Meteorol. Soc.* **98**, 737–752 (2017). doi:10.1175/BAMS-D-16-0057.1

14. F. Li, M. S. Lozier, W. E. Johns, Calculating the meridional volume, heat, and freshwater transports from an observing system in the subpolar North Atlantic: Observing system simulation experiment. *J. Atmos. Ocean. Technol.* **34**, 1483–1500 (2017). doi:10.1175/JTECH-D-16-0247.1

15. M. F. de Jong, L. de Steur, Strong winter cooling over the Irminger Sea in winter 2014–2015, exceptional deep convection, and the emergence of anomalously low SST. *Geophys. Res. Lett.* **43**, 7106–7113 (2016). doi:10.1002/2016GL069596

16. A. Piron, V. Thierry, H. Mercier, G. Caniaux, Gyre-scale deep convection in the subpolar North Atlantic Ocean during winter 2014-2015. *Geophys. Res. Lett.* **44**, 1439–1447 (2017). doi:10.1002/2016GL071895

17. F. Fröb, A. Olsen, K. Våge, G. W. K. Moore, I. Yashayaev, E. Jeansson, B. Rajasakaren, Irminger Sea deep convection injects oxygen and anthropogenic carbon to the ocean interior. *Nat. Commun.* **7**, 13244 (2016). doi:10.1038/ncomms13244 Medline

18. I. Yashayaev, J. W. Loder, Further intensification of deep convection in the Labrador Sea in 2016. *Geophys. Res. Lett.* **44**, 1429–1438 (2017). doi:10.1002/2016GL071668

19. X. Xu, E. P. Chassignet, W. E. Johns, W. J. Schmitz Jr., E. J. Metzger, Intraseasonal to interannual variability of the Atlantic meridional overturning circulation from eddy-resolving simulations and observations. *J. Geophys. Res. Oceans* **119**, 5140–5159 (2014). doi:10.1002/2014JC009994

20. N. P. Holliday, S. Bacon, S. A. Cunningham, S. F. Gary, J. Karstensen, B. A. King, F. Li, E. L. Mcdonagh, Subpolar North Atlantic overturning and gyre-scale circulation in the summers of 2014 and 2016. *J. Geophys. Res. Oceans* **123**, 4538–4559 (2018). doi:10.1029/2018JC013841

21. D. A. Smeed, S. A. Josey, C. Beaulieu, W. E. Johns, B. I. Moat, E. Frajka-Williams, D. Rayner, C. S. Meinen, M. O. Baringer, H. L. Bryden, G. D. McCarthy, The North Atlantic Ocean is in a state of reduced overturning. *Geophys. Res. Lett.* **45**, 1527–1533 (2018). doi:10.1002/2017GL076350

22. H. Mercier, P. Lherminier, A. Sarafanov, F. Gaillard, N. Daniault, D. Desbruyères, A. Falina, B. Ferron, C. Gourcuff, T. Huck, V. Thierry, Variability of the meridional overturning circulation at the Greenland-Portugal OVIDE section from 1993 to 2010. *Prog. Oceanogr.* **132**, 250–261 (2015). doi:10.1016/j.pocean.2013.11.001

23. M. A. Spall, Boundary currents and watermass transformation in marginal seas. *J. Phys. Oceanogr.* **34**, 1197–1213 (2004). doi:10.1175/1520-0485(2004)034<1197:BCAWTI>2.0.CO;2

24. F. Straneo, On the connection between dense water formation, overturning, and poleward heat transport in a convective basin. *J. Phys. Oceanogr.* **36**, 1822–1840 (2006). doi:10.1175/JPO2932.1

25. R. S. Pickart, M. A. Spall, Impact of Labrador Sea convection on the North Atlantic meridional overturning circulation. *J. Phys. Oceanogr.* **37**, 2207–2227 (2007). doi:10.1175/JPO3178.1

26. G. D. McCarthy, D. A. Smeed, W. E. Johns, E. Frajka-Williams, B. I. Moat, D. Rayner, M. O. Baringer, C. S. Meinen, J. Collins, H. L. Bryden, Measuring the Atlantic meridional overturning circulation at 26°N. *Prog. Oceanogr.* **130**, 91–111 (2015). doi:10.1016/j.pocean.2014.10.006

27. G. Danabasoglu, S. G. Yeager, D. Bailey, E. Behrens, M. Bentsen, D. Bi, A. Biastoch, C. Böning, A. Bozec, V. M. Canuto, C. Cassou, E. Chassignet, A. C. Coward, S. Danilov, N. Diansky, H. Drange, R. Farneti, E. Fernandez, P. G. Fogli, G. Forget, Y. Fujii, S. M. Griffies, A. Gusev, P. Heimbach, A. Howard, T. Jung, M. Kelley, W. G. Large, A. Leboissetier, J. Lu, G. Madec, S. J. Marsland, S. Masina, A. Navarra, A. J. George Nurser, A. Pirani, D. S. y Mélia, B. L. Samuels, M. Scheinert, D. Sidorenko, A.-M. Treguier, H. Tsujino, P. Uotila, S. Valcke, A. Voldoire, Q. Wang, North Atlantic simulations in coordinated ocean-ice reference experiments phase II (CORE-II). Part I: Mean states. *Ocean Model.* **73**, 76–107 (2014). doi:10.1016/j.ocemod.2013.10.005

28. J. Holte, F. Straneo, Seasonal overturning of the Labrador Sea as observed by Argo floats. *J. Phys. Oceanogr.* **47**, 2531–2543 (2017). doi:10.1175/JPO-D-17-0051.1

29. A. Sarafanov, A. Falina, H. Mercier, A. Sokov, P. Lherminier, C. Gourcuff, S. Gladyshev, F. Gaillard, N. Daniault, Mean full-depth summer circulation and transports at the northern periphery of the Atlantic Ocean in the 2000s. *J. Geophys. Res. Oceans* **117**, C01014 (2012).

30. T. Rossby, G. Reverdin, L. Chafik, H. Søiland, A direct estimate of poleward volume, heat, and freshwater fluxes at 59.5°N between Greenland and Scotland. *J. Geophys. Res. Oceans* **122**, 5870–5887 (2017). doi:10.1002/2017JC012835

31. K. E. Trenberth, J. M. Caron, Estimates of meridional atmosphere and ocean heat transports. *J. Clim.* **14**, 3433–3443 (2001). doi:10.1175/1520-0442(2001)014<3433:EOMAAO>2.0.CO;2

32. R. Zantopp, J. Fischer, M. Visbeck, J. Karstensen, From interannual to decadal: 17 years of boundary current transports at the exit of the Labrador Sea. *J. Geophys. Res. Oceans* **122**, 1724–1748 (2017). doi:10.1002/2016JC012271

33. S. Zou, M. S. Lozier, Breaking the linkage between Labrador Sea Water production and its advective export to the subtropical gyre. *J. Phys. Oceanogr.* **46**, 2169–2182 (2016). doi:10.1175/JPO-D-15-0210.1

34. C. Eden, J. Willebrand, Mechanism of interannual to decadal variability of the North Atlantic circulation. *J. Clim.* **14**, 2266–2280 (2001). doi:10.1175/1520-0442(2001)014<2266:MOITDV>2.0.CO;2

35. D. A. Bailey, P. B. Rhines, S. Häkkinen, Formation and pathways of North Atlantic Deep Water in a coupled ice–ocean model of the Arctic–North Atlantic Oceans. *Clim. Dyn.* **25**, 497–516 (2005). doi:10.1007/s00382-005-0050-3

36. J. Getzlaff, C. W. Böning, C. Eden, A. Biastoch, Signal propagation related to the North Atlantic overturning. *Geophys. Res. Lett.* **32**, L09602 (2005). doi:10.1029/2004GL021002

37. G. Danabasoglu, S. G. Yeager, Y.-O. Kwon, J. J. Tribbia, A. S. Phillips, J. W. Hurrell, Variability of the Atlantic meridional overturning circulation in CCSM4. *J. Clim.* **25**, 5153–5172 (2012). doi:10.1175/JCLI-D-11-00463.1

38. J. Robson, P. Ortega, R. Sutton, A reversal of climatic trends in the North Atlantic since 2005. *Nat. Geosci.* **9**, 513–517 (2016). doi:10.1038/ngeo2727

39. L. C. Jackson, K. A. Peterson, C. D. Roberts, R. A. Wood, Recent slowing of Atlantic overturning circulation as a recovery from earlier strengthening. *Nat. Geosci.* **9**, 518–522 (2016). doi:10.1038/ngeo2715

40. D. J. R. Thornalley, D. W. Oppo, P. Ortega, J. I. Robson, C. M. Brierley, R. Davis, I. R. Hall, P. Moffa-Sanchez, N. L. Rose, P. T. Spooner, I. Yashayaev, L. D. Keigwin, Anomalously weak Labrador Sea convection and Atlantic overturning during the past 150 years. *Nature* **556**, 227–230 (2018). doi:10.1038/s41586-018-0007-4 Medline

41. F. Li, M. S. Lozier, On the linkage between Labrador Sea Water volume and overturning circulation in the Labrador Sea: A case study on proxies. *J. Clim.* **31**, 5225–5241 (2018). doi:10.1175/JCLI-D-17-0692.1

42. M. Bersch, I. Yashayaev, K. P. Koltermann, Recent changes of the thermohaline circulation in the subpolar North Atlantic. *Ocean Dyn.* **57**, 223–235 (2007). doi:10.1007/s10236-007-0104-7

43. K. Våge, R. S. Pickart, A. Sarafanov, Ø. Knutsen, H. Mercier, P. Lherminier, H. M. van Aken, J. Meincke, D. Quadfasel, S. Bacon, The Irminger Gyre: Circulation, convection, and interannual variability. *Deep Sea Res. Part I Oceanogr. Res. Pap.* **58**, 590–614 (2011). doi:10.1016/j.dsr.2011.03.001

44. N. P. Holliday, S. A. Cunningham, C. Johnson, S. F. Gary, C. Griffiths, J. F. Read, T. Sherwin, Multidecadal variability of potential temperature, salinity, and transport in the eastern subpolar North Atlantic. *J. Geophys. Res. Oceans* **120**, 5945–5967 (2015). doi:10.1002/2015JC010762

45. I. Yashayaev, J. W. Loder, Recurrent replenishment of Labrador Sea Water and associated decadal-scale variability. *J. Geophys. Res. Oceans* **121**, 8095–8114 (2016). doi:10.1002/2016JC012046

46. Argo, Argo float data and metadata from Global Data Assembly Centre (Argo GDAC), SEANOE (2018); https://doi.org/10.17882/42182.

47. M. S. Lozier, F. Li, S. Bacon, F. Bahr, A. S. Bower, S. A. Cunningham, M. F. de Jong, L. de Steur, B. deYoung, J. Fischer, S. F. Gary, B. J. W. Greenan, N. P. Holliday, A. Houk, L. Houpert, M. E. Inall, W. E. Johns, C. Johnson, J. Karstensen, G. Koman, I. A. Le Bras, X. Lin, N. Mackay, M. Oltmanns, R. S. Pickart, A. L. Ramsey, D. Rayner, F. Straneo, D. J. Torres, I. Yashayaev, J. Zhao, Meridional Overturning Circulation and the Associated Heat and Freshwater Transports Observed by the OSNAP Array from 2014 to 2016, Duke Digital Repository (2019); https://doi.org/10.7924/r4z60gf0f.

48. J. Karstensen, M. Oltmanns, OSNAP mooring data recovered during MSM54, PANGAEA (2018); https://doi.pangaea.de/10.1594/PANGAEA.896648.

49. Data Collection - OSNAP, Version OSNAP-V2-2018, Zenodo (2018); https://doi.org/10.5281/zenodo.1285757.

50. R. Pickart, Microcat, Aquadopp, ADCP, and Tidbit data from the 2014-2016 Labrador Sea eastern boundary mooring array as part of OSNAP, Duke Digital Repository (2018); https://doi.org/10.7924/r4fj2dr7k.

51. F. Straneo, A. Ramsey, F. Bahr, D. Torres, Microcat, current meter and ADCP data from the Cape Farewell mooring array southeast of Greenland as part of OSNAP, Duke Digital Repository (2018); https://doi.org/10.7924/r4fb50z9b.

52. N. P. Holliday, D. Rayner, S. Bacon, L. Houpert, Microcat, current meter and ADCP data from moorings of the Deep Western Boundary Current array (Irminger Sea) as part of UK OSNAP, British Oceanographic Data Centre - Natural Environment Research Council, UK (2018); https://doi.org/10/cwf4.

53. L. de Steur, M. F. de Jong, High-resolution current meter and hydrographic data from the Irminger Current mooring array 2014-2015, NIOZ Royal Netherlands Institute for Sea Research (2018); https://doi.org/10.4121/uuid:77b2c4fc-c253-4494-91bd-8d1ef66a014a.

54. L. de Steur, M. F. de Jong, High-resolution current meter and hydrographic data from the Irminger Current mooring array 2015-2016, NIOZ Royal Netherlands Institute for Sea Research (2018); https://doi.org/10.4121/uuid:9ae97ceb-39e4-43ec-abdb-614103285c16.

55. W. Johns, A. Houk, Microcat, current meter and ADCP data from the eastern mid-Atlantic ridge mooring array as part of OSNAP, Duke Digital Repository (2018); https://doi.org/10.7924/r42n52w51.

56. J. Zhao, A. Bower, J. Yang, X. Lin, CTD data collected by Slocum glider operated between June and November 2015 in the Iceland Basin as part of OSNAP, Duke Digital Repository (2018); https://doi.org/10.7924/r4m905g03.

57. L. Houpert, M. E. Inall, E. Dumont, S. A. Cunningham, UK OSNAP near real-time glider dataset, British Oceanographic Data Centre - Natural Environment Research Council, UK (2018); https://doi.org/10/ckbr.

58. S. A. Cunningham, L. Houpert, E. Dumont, M. E. Inall, Microcat, current meter and ADCP data from moorings of the Eastern Boundary array (Rockall Trough) as part of UK OSNAP, British Oceanographic Data Centre - Natural Environment Research Council, UK (2018); https://doi.org/10/cwf3.

59. R. A. Locarnini, A. V. Mishonov, J. I. Antonov, T. P. Boyer, H. E. Garcia, O. K. Baranova, M. M. Zweng, C. R. Paver, J. R. Reagan, D. R. Johnson, M. Hamilton, D. Seidov, *World Ocean Atlas 2013, Volume 1: Temperature*, S. Levitus, Ed.; A. Mishonov, Technical Ed. (NOAA Atlas NESDIS 73, 2013); https://repository.library.noaa.gov/view/noaa/14847.

60. M. M. Zweng, J. R. Reagan, J. I. Antonov, R. A. Locarnini, A. V. Mishonov, T. P. Boyer, H. E. Garcia, O. K. Baranova, D. R. Johnson, D. Seidov, M. M. Biddle, *World Ocean Atlas 2013, Volume 2: Salinity*, S. Levitus, Ed.; A. Mishonov, Technical Ed. (NOAA Atlas NESDIS 74, 2013); https://repository.library.noaa.gov/view/noaa/14848.

61. D. P. Dee, S. M. Uppala, A. J. Simmons, P. Berrisford, P. Poli, S. Kobayashi, U. Andrae, M. A. Balmaseda, G. Balsamo, P. Bauer, P. Bechtold, A. C. M. Beljaars, L. van de Berg, J. Bidlot, N. Bormann, C. Delsol, R. Dragani, M. Fuentes, A. J. Geer, L. Haimberger, S. B. Healy, H. Hersbach, E. V. Hólm, L. Isaksen, P. Kållberg, M. Köhler, M. Matricardi, A. P. McNally, B. M. Monge-Sanz, J.-J. Morcrette, B.-K. Park, C. Peubey, P. de Rosnay, C. Tavolato, J.-N. Thépaut, F. Vitart, The ERA-Interim reanalysis: Configuration and performance of the data assimilation system. *Q. J. R. Meteorol. Soc.* **137**, 553–597 (2011). doi:10.1002/qj.828

62. C. Gourcuff, P. Lherminier, H. Mercier, P. Y. Le Traon, Altimetry combined with hydrography for ocean transport tstimation. *J. Atmos. Ocean. Technol.* **28**, 1324–1337 (2011). doi:10.1175/2011JTECHO818.1

63. T. J. Sherwin, D. Aleynik, E. Dumont, M. E. Inall, Deep drivers of mesoscale circulation in the central Rockall Trough. *Ocean Sci.* **11**, 343–359 (2015). doi:10.5194/os-11-343-2015

64. C. W. Böning, M. Scheinert, J. Dengg, A. Biastoch, A. Funk, Decadal variability of subpolar gyre transport and its reverberation in the North Atlantic overturning. *Geophys. Res. Lett.* **33**, L21S01 (2006). doi:10.1029/2006GL026906

65. G. Han, Z. Ma, Z. Long, W. Perrie, J. Chassé, Climate change on Newfoundland and Labrador shelves: Results from a regional downscaled ocean and sea-ice model under an A1B forcing scenario 2011–2069. *Atmosphere-Ocean* 10.1080/07055900.2017.1417110 (2018). doi:10.1080/07055900.2017.1417110

66. B. Curry, C. M. Lee, B. Petrie, R. E. Moritz, R. Kwok, Multiyear volume, liquid freshwater, and sea ice transports through Davis Strait, 2004-10. *J. Phys. Oceanogr.* **44**, 1244–1266 (2014). doi:10.1175/JPO-D-13-0177.1

67. R. A. Woodgate, Increases in the Pacific inflow to the Arctic from 1990 to 2015, and insights into seasonal trends and driving mechanisms from year-round Bering Strait mooring data. *Prog. Oceanogr.* **160**, 124–154 (2018). doi:10.1016/j.pocean.2017.12.007

68. M. M. Hall, H. L. Bryden, Direct estimates and mechanisms of ocean heat-transport. *Deep Sea Res. Part I Oceanogr. Res. Pap.* **29**, 339–359 (1982). doi:10.1016/0198-0149(82)90099-1

69. W. E. Johns, M. O. Baringer, L. M. Beal, S. A. Cunningham, T. Kanzow, H. L. Bryden, J. J. M. Hirschi, J. Marotzke, C. S. Meinen, B. Shaw, R. Curry, Continuous, Array-based estimates of Atlantic Ocean heat transport at 26.5°N. *J. Clim.* **24**, 2429–2449 (2011). doi:10.1175/2010JCLI3997.1

70. R. E. Thomson, W. J. Emery, "Time-series analysis methods" in *Data Analysis Methods in Physical Oceanography* (Elsevier Science, 2014), chap. 5.

71. D. R. Jackett, T. J. McDougall, A neutral density variable for the world's oceans. *J. Phys. Oceanogr.* **27**, 237–263 (1997). doi:10.1175/1520-0485(1997)027<0237:ANDVFT>2.0.CO;2

72. E. L. McDonagh, B. A. King, H. L. Bryden, P. Courtois, Z. Szuts, M. Baringer, S. A. Cunningham, C. Atkinson, G. McCarthy, Continuous estimate of Atlantic oceanic freshwater flux at 26.5°N. *J. Clim.* **28**, 8888–8906 (2015). doi:10.1175/JCLI-D-14-00519.1